Contemporary Mathematics
https://ojs.wiserpub.com/index.php/CM/

Research Article

Impacts of Viscous Dissipation and Nanoparticle Flow in Pressure-Driven Hydrosphere and Atmosphere Interface on Climate Change: A Numerical Perspective

Hossam A. Nabwey[1]*, Rabia Iqbal[2], Muhammad Ashraf[2], A. M. Rashad[3], Abdullah Aldurayhim[1], M. M. Nour[1]

[1] Department of Mathematics, College of Science and Humanities in Al-Kharj, Prince Sattam bin Abdulaziz University, Al-Kharj 11942, Saudi Arabia
[2] Department of Mathematics, Faculty of Science, University of Sargodha, Sargodha 40100, Pakistan
[3] Department of Mathematics, Aswan University, Faculty of Science, Aswan 81528, Egypt
E-mail: h.mohamed@psau.edu.sa

Received: 21 October 2025; **Revised:** 22 January 2026; **Accepted:** 23 January 2026

Abstract: The effects of natural convection heat transfer from the hydrosphere to the atmosphere are investigated numerically on the climate in current work under the assumptions that the hydrosphere phase is influenced by viscous dissipation and that there is an evaporation region at its surface where density is pressure dependent. Furthermore, the impacts of atmospheric nanoparticles are examined using Buongiorno's Model. This is carried out by constructing a two-dimensional mathematical model in the form of a spherical coordinate system that includes three regions: the hydrosphere, the evaporation and the atmosphere, connected through trans-boundaries. To better comprehend the physical importance of the proposed study, the system of governing equations is altered into a dimensionless system using a set of relevant variables and numerically answered using the finite difference approach via primitive variable formulation and the Gaussian elimination scheme. The consequences of numerous dimensionless variables, such as the viscous dissipation parameter in the hydrosphere, the density variation parameter in the evaporation region and the Brownian motion parameter and the thermophoresis parameter in the atmospheric region, are seen on climate patterns. The radial distribution of temperature across the hydrosphere, evaporation zone, and atmosphere is observed using concentric contour plots for Grashof number $Gr = 8$ and 20. The results indicate a distinct negative temperature gradient, with the highest thermal intensity at the hydrosphere and progressively lower values toward the outer atmospheric region, highlighting steady radial heat transfer through the evaporation zone.

***Keywords*:** natural convection, concentric spheres, viscous dissipation, atmosphere, hydrosphere, evaporation, transboundary, nanofluids

MSC: 76U05, 76W05, 76D05

Nomenclature

Pr	Prandtl number

DOI: https://doi.org/10.37256/cm.7320268961

Gr Grashof number
Gr_T Thermal Grashof number for atmosphere
Gr_C Concentration Grashof quantity for atmosphere
C_p Specific heat ($Jkg^{-1}K^{-1}$)
g Gravitational acceleration (ms^{-2})
P Pressure of fluid
T Temperature (K)
C Nanoparticle concentration expansion coefficient
D_B Brownian diffusion coefficient (m^2s^{-1})
D_T Thermophoresis diffusion coefficient (m^2s^{-1})
T_∞ Ambient temperature
T_w Hydrosphere surface temperature (K)
T_E Evaporation surface temperature (K)
T_A Atmosphere surface temperature (K)
k Thermal conductivity ($Wm^{-1}K^{-1}$)
N_t Brownian motion parameter
N_b Thermophoresis parameter

Greek letters

ϕ Non-dimensional temperature
β_C Concentration expansion coefficient
β Thermal expansion coefficient (K^{-1})
λ_E Density variation parameter for evaporation phase
ξ Nanoparticles concentration
ψ Dimensionless pressure
ν Kinematic viscosity (m^2s^{-1})
μ Dynamic viscosity (Nsm^{-2})
ρ Density (kgm^{-3})
β_A Atmospheric density variation parameter
ε_A Atmospheric viscosity variation parameter
η_A Atmospheric thermal conductivity variation parameter
Ω Viscous dissipation parameter
α Thermal diffusivity (m^2s^{-1})
γ Location representative (angle)

Subscripts

A Atmosphere region
H Hydrosphere region
E Evaporation region

1. Introduction

Weather dynamics, energy transfer, and the global hydrological cycle are strongly influenced by interactions between the hydrosphere and the atmosphere, which play a central role in regulating the Earth's climate system. In particular, viscous dissipation within the hydrosphere alters local temperature gradients and convective flow structures by converting kinetic energy into thermal energy, thereby contributing to localized heating effects. Simultaneously, pressure-induced density variations near the hydrosphere-atmosphere interface influence evaporation rates, buoyancy forces, and vapor diffusion

processes. Moreover, the presence of suspended nanoparticles in the atmospheric layer modifies thermal conductivity and radiative transport characteristics, further affecting interfacial energy exchange. A quantitative understanding of these coupled mechanisms, namely viscous heating in water, pressure-dependent density behavior in air, and nanoparticle-enhanced thermal transport, is essential for developing accurate surface-atmosphere interaction models. Such improvements enhance the representation of heat-exchange feedback mechanisms and contribute to more reliable climate prediction frameworks relevant to climate change mitigation.

A result for steady axisymmetric convection from nature between thermally similar spheres with common center was developed by Mack and Hardee [1] by treating all fluid properties as constants, with the exception of specific weight, and neglecting viscous heating. Free convection between two thermally comparable concentric spheres with ratios of diameters varying from 1.09 to 2.81 was examined experimentally by Scanlan et al. [2]. The results of an experimental and numerical investigation of convection flow that naturally occurs within horizontal isothermal concentric cylinders were published by Kuehn and Goldstein [3]. For instance, local heat-transfer coefficients and heat distributions are experimentally determined values. An effective finite difference approach combined with the cubic spline interpolation methodology was utilized by Lee et al. [4] to produce numerical solutions for the variation of the wall temperature for thin cylinders and needles with a curvature parameter. In [5], Chamkha investigates the unsteady, uniform double-diffusive convective circulation of a binary combination of gases in a rectangular enclosure with a temperature-dependent energy source or sink and a homogenous permeable material. Asbik et al. [6] studied continuous laminar mixed convection mathematically in a fluid-saturated, pointing upward, homogeneous permeable enclosure. Temperature and concentration gradients on the vertical walls are the source of the buoyant forces that drive the fluid motion. Alam et al. [7] described the effects of viscous dissipation on magneto-hydrodynamic natural convection movement across a sphere in the setting of heat generation. The impacts of an atmospheric pressure on natural convection heat transfer from the horizontal cylindrical specimen were experimentally investigated by Saidi and Abardeh [8]. By solving three-dimensional Boussinesq equations with dimensionless variables such as temperature, vorticity vector, and vector potential functions, Sheremet [9] theoretically reproduced transient natural convection heat transport zones within a sphere. Using the Buongiorno model, Khan and Uddin [10] have investigated the consequences of thermophoresis and Brownian motion on the flow, temperature, and mass transfer off a regular plate with a given surface heat flux. By connecting some of the methodologies and concepts used in many fields involved with the phenomenon of evaporation in the natural environment, Brutsaert in [11] improved our understanding of evaporation. Parveen et al. [12] explored the effect of viscous dissipation upon the natural convection movement considering a viscous incompressible fluid next to a vertically wavy, evenly heated surface. Garoosi et al. [13] investigated the natural convection heat transport of nanofluid numerically in a two-dimensional square cavity that included several heater-cooler pairs. Numerous collections of isothermal-walled heaters and coolers are installed inside the cavity, which has insulated walls. In [14], Lappa discussed how a deviation from the known behavior of gases at normal temperatures can impact the flow and how to suitably extend a standard numerical framework for compressible flows with low Mach numbers to simulate thermal flows at high temperatures. A mathematical model was created by Kazemi et al. [15] to explain how the transport processes at the interface are coupled with the momentum, mass and heat transfer in the fluids. In evaporation from a concave meniscus for different vacuum pressures, the model was utilized to comprehend the temperature profiles in the liquid and vapor as well as the experimentally acquired velocity field in the liquid. The infinite spinning disk problem was resolved by Mustafa [16] in the scenario when a nanofluid which is electrically conducting is present in the space above the rough disk. Brownian motion and thermophoresis effects caused by nanoparticles are incorporated using the Buongiorno model. Ashraf and Fatima [17] introduced the matter of periodic convective flow around various sphere points when viscous dissipation is present. Considering the impact of viscous dissipation in the energy equation, Ahmad et al. [18] investigated the flow of an incompressible micro-polar fluid with mass and heat transfer via a resistive permeable medium between planar channel walls. Iasiello et al. [19] explored the impact of both hypo-and hyperthermia on a bent artery. The heat source or sink is applied from the inside of the artery (the lumen side). The curvature effect of the artery is represented by the change in the arterial curvature ratio, whereas the wall is modeled with a multilayer model that addresses the different properties of the various layers. The collective process of mixed convection flow and thermo-phoretic transport along the sphere's surface was investigated by Abbas et al. [20]. Khan et al. [21] examined the physical phenomenon of fluid outbreak through a boundary layer into a plume area above the sphere's

surface and free convection Nano-fluid heat transfer along a sphere. They also examined the impact of heat generation when an applied magnetic field was included. In the context of viscous dissipation via a porous media, Mishra and Kumar [22] investigated mass transfer, procreative or absorptive temperature, and magneto-hydrodynamic flow of Nano-fluid current across a wedge. Heat transfer properties and natural convection flow of Buongiorno's mathematical model Nano-fluid flow within a square cavity with adiabatic surroundings on the top and bottom walls and isothermal surroundings on both side walls were examined by Reddy and Sreedevi [23]. Using Buongiorno's Nano-fluid, Khatun and Nasreen [24] numerically modeled free convective flow within the trapezoidal zone with oscillatory materials and temperature distributions at both inclined boundaries. Akhter and Ashraf [25] created a mathematical model for the bio-convection movement of a Nano-fluid immersed in a Darcy-Forchheimer medium with a nonlinear stretchable surface. In order to account for slip flow, Ashraf et al. [26] examined the implications of viscous dissipation and thermos-phoretic motion on the two-dimensional fluid traveling along various spherical positions. Ashraf et al. [27] investigated the cyclical behavior of convective heat transfer features of fluid current across an electrically conductive cone implanted in the permeable environment by introducing viscous dissipation effects into the energy equation. Nadeem et al. [28] discussed the effects of thermophoresis and Brownian motion with viscous dissipation, as well as the viscoelastic fluid flow across a nonlinear expanding porous sheet with suction and injection. Heat transmission characteristics of copper or water Nano-fluid flow across a dual-direction stretched sheet were theoretically examined by Owhaib and Al-Kouz [29]. Begum et al. [30] used numerical simulations to investigate how the unstable natural convection flow of a Newtonian fluid that is incompressible into a rectangular chamber is affected by viscous dissipation and continuous volumetric heat generation. Ullah et al. [31] investigated how the mass and heat transport of reacting chemicals and magnetic nanofluids over the stretched sheet were affected by a detailed analysis of thermal density, viscosity dissipation, chemical reaction, and thermophoresis. Ashraf et al. [32] investigated the physical effects of thermal radiation on heat and mass transmission in a nanofluid round a sphere. NematpourKeshteli et al. [33] conducted a simulation that demonstrated the possibility of simultaneous harvesting and storing of solar thermal energy via a lobed double-pipe heat exchanger with Phase Change Materials (RT82) in a solar collector energy storage unit. NematpourKeshteli et al. [34] suggested remedies for enhancing the heat-flow-characteristic of paraffin used as a Phase Change Material (PCM) in solar flat-plate collector systems for both home and industrial solar uses. Ramirez et al. [35] introduced a hygro-thermo-mechanical model, which was used as a tool to simulate the effect of temperature and moisture-related phenomena on the mechanical performance of masonry walls. They also presented a fully-coupled heat and mass transfer model and prepared a 2D finite element model to investigate the reaction of a brick masonry wall under different hygro-thermal conditions. Khan et al. [36] focused on the MHD second-grade nanofluid flow with produced magnetic field and viscous dissipation on an exponentially stretched surface. The solutal and thermal energy equations were investigated in the context of fluctuating thermal conductivity and the thermophoretic effect. The consequences of Carreau fluid flow along a curved stretch surface were thoroughly examined in a study by Ullah et al. [37]. Numerous factors, including viscous dissipation, convective boundary conditions, thermophoresis, nonlinear thermal radiation, Brownian motion, and nonlinear mixed convection, are meticulously considered in this paper. Khan et al. [38] investigated nonlinear mixed convection in magnetohydrodynamic nanomaterial flows. The flow across the stretching barrier is computed. Melting of heat is investigated. Heat generation, radiation, and Joule heating are all taken into consideration by the thermal equation. The Arrhenius activation energy of chemical processes is examined. Random motion and thermophoresis properties are examined. NematpourKeshteli et al. [39] investigators focused on utilizing heat transfer improvement methods, including nanoparticles, porous metal foams, and extended surfaces, for the thermal energy storage system of a flat plate solar collector based on Phase Change Material (PCM). With a focus on climate change, Nadeem et al. [40] investigated the effects of thermophoretic particles produced during the combustion of fossil fuels in a bi-stratified atmosphere with thermal sinks in the plume region and catalytic reactions taking place in the source zone. The implications of oscillating thermal waves on convective heat transfer in the presence of a heat source and sink have been thoroughly addressed by Rehman et al. [41]. In order to describe the complex, non-linear nature of vorticity, heat transfer, and fluid flow, the study begins by creating the momentum, heat, and continuity equations. Nabwey et al.'s study of the origins and consequences of convective transport of heat in humid air [42] demonstrated the phenomenon's importance in a variety of physical contexts, such as climate research, engineering, and meteorology. Imtiaz et al.'s work [43] looks at a hybrid nanofluid for convective heat transfer along the surface of an inclined hemisphere and its effect on climate

change. In order to demonstrate how different hydrosphere and atmosphere densities affect climate change, Iqbal et al. [44] employed thermal jump effects in the atmosphere area. Iqbal et al. [45] emphasized the impact of the hydrosphere's and the porous atmosphere's varying thermal conductivity and viscosity on climate change. Shahraki et al. [46] investigated the charging performance upgrade in a Triplex-Tube latent Heat thermal energy storage system (TTHX) that features the addition of longitudinal fins and alumina nanoparticles in Phase Change Materials (PCMs). They carry out numerical simulations that establish the systematic consideration of not only fin length, thickness, number, and orientation but also the effect of Nano-Enhanced PCMs (NEPCMs) in coming up with the best configurations for enhanced charging performance.

Thermophoresis, apart from being a primary factor in the movement of nanoparticles, is a very important mechanism in almost all practical engineering applications. Its influence is seen in medicine as well [19]. Thermophoretic forces guide the movement of nanoparticles in the delivery of heat-based drugs and other treatments. In building and environmental engineering, thermophoresis causes a change in the deposition of aerosols, indoor air quality, and the transfer of heat through surfaces that are heated. In addition, their ability to transfer the heat of the particles has found applications in solar energy systems, heat exchangers, and electronics cooling devices, where temperature-gradient-driven particle motion enhances effective thermal conductivity and energy transport. The present study, inspired by these applications, integrates thermophoresis into a hydrosphere-atmosphere framework to see how nanoparticle-induced thermal transport may affect the heat exchange processes at the interface which are significant for the energy balance of the climate.

The objective of this study is to bridge this gap by examining the integrated effects of these three parameters, providing a more comprehensive understanding of the thermal interaction at the atmosphere and waterbodies interface and Earth's energy balance. The current research has taken a step further in the area of climate change mitigation by conducting a numerical study that has revealed the role of pressure gradients, viscous dissipation, evaporation, and the presence of nanoparticles in the interfacial heat exchange. These processes have a direct impact on the global warming of the surface, the positioning of the different air masses, and the thermal feedback loop. By improving the physical understanding of these coupled transport phenomena, the proposed model supports the development of more reliable climate prediction frameworks and mitigation-oriented thermal regulation strategies.

2. Analytical structure and basic equations

Thermal interaction between the hydrosphere and the atmosphere is a natural phenomenon. Compared to the atmosphere, the hydrosphere absorbs more heat from incoming solar radiation. Heat is transferred by evaporation from the warmer hydrosphere to the cooler atmosphere across the hydrosphere-atmosphere interface. Figure 1 illustrates the two-dimensional, axisymmetric geometry of the spherical coordinate system under consideration, consisting of three concentric regions. The velocity components in the r and θ directions are denoted by u_r and u_θ, respectively. The inner sphere represents the hydrosphere surface at temperature $T = T_w$, which is connected via interfacial boundaries to the evaporation zone at temperature $T = T_E$, and subsequently to the atmospheric region at temperature $T = T_A$. By natural convention, the temperatures satisfy $T_w > T_E$ and $T_E > T_A$.

The concentric spherical geometry utilized in this research is meant to describe a perfect case of hydrosphere-atmosphere interaction in which heat and mass are mainly transferred in the radial direction from a large water body to the air. Such a layout is particularly appropriate for the average thermal exchange processes modeling over lakes, reservoirs, or small oceanic regions, where the effects of curvature are significant and the azimuthal variations are relatively small. The assumption of symmetry around the axis simplifies the problem to radial and angular transport while ignoring edge effects, which is a reasonable assumption when the characteristic length scale of the hydrosphere is significantly larger than the thermal boundary layer thickness. This method is in line with previous investigations into natural convection between concentric spheres and spherical surfaces, where the main aim is to separate buoyancy-driven and interfacial heat transfer mechanisms under controlled geometric conditions.

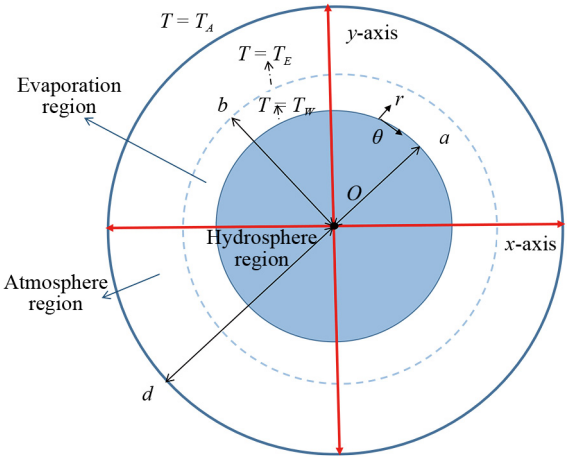

Figure 1. Schematic diagram of hydrosphere-atmosphere interface

2.1 *Hydrosphere region*

In this study, the hydrosphere zone is considered to be influenced by viscous dissipation, which converts kinetic energy into heat due to internal friction within the fluid. This effect is particularly important in boundary layers near the hydrosphere surface, where it can significantly alter the thermal behavior of water bodies. The hydrosphere is modeled as a sphere of radius a and is assumed to be incompressible, with uniform density, viscosity, and thermal conductivity. The temperature at the surface of the evaporation zone, T_E serves as the ambient temperature for the hydrosphere, establishing a thermal connection between the two regions through interfacial boundaries. Following the approaches outlined in [39, 40], the dimensionless governing equations for this flow configuration are provided below.

$$\frac{\partial \hat{u}_r}{\partial \hat{r}} + \frac{1}{\sin\hat{\theta}} \frac{\partial \left(\sin\hat{\theta}\hat{u}_\theta\right)}{\partial \hat{\theta}} = 0, \tag{1}$$

$$\hat{u}_r \frac{\partial \hat{u}_\theta}{\partial \hat{r}} + \hat{u}_\theta \frac{\partial \hat{u}_\theta}{\partial \hat{\theta}} = \frac{\partial^2 \hat{u}_\theta}{\partial \hat{r}^2} \pm Gr_H \phi \cos\gamma, \tag{2}$$

$$\hat{u}_r \frac{\partial \phi}{\partial \hat{r}} + \hat{u}_\theta \frac{\partial \phi}{\partial \theta} = \frac{1}{Pr_H} \frac{\partial^2 \phi}{\partial \hat{r}^2} + \Omega \left(\frac{\partial \hat{u}_\theta}{\partial \hat{r}}\right)^2, \tag{3}$$

constrained on boundary conditions

$$\begin{aligned} &\hat{u}_\theta = 0, \quad \hat{u}_r = 0, \quad \phi = 1, \text{ at } \hat{r} = 0, \\ &\hat{u}_\theta \to 0, \quad \phi \to 0, \text{ as } \hat{r} \to \infty, \end{aligned} \tag{4}$$

where $Pr_H = \dfrac{\nu}{\alpha}$, $Gr_H = \dfrac{g\beta\left(T_w - T_E\right)a^3}{\upsilon^2}$ and $\Omega = \dfrac{\upsilon^2}{\Delta T a^2 C_p}$ are Prandtl, Grashof and viscous dissipation constant respectively.

2.1.1 *Methodological framework and computational strategy*

The present problem is solved using the finite difference method. The governing equations (1)–(4) are first expressed in a suitable form through the primitive variable formulation. These differential equations are then discretized using the finite difference approach, which transforms them into a system of algebraic equations. The procedure follows the methodology outlined in [39], resulting in the algebraic system presented below.

$$U_{r_{(i+1,\ j)}} = U_{r_{(i-1,\ j)}} + \frac{R_j}{4}\left(U_{\theta_{(i+1,\ j)}} - U_{\theta_{(i-1,\ j)}}\right) - \Delta R U_{\theta_{(i,\ j)}} - 2\Delta R\Theta_i U_{\theta_{(i,\ j)}} \cot\Theta_i - \frac{2\Delta R\Theta_i}{\Delta\Theta}\left(U_{\theta_{(i,\ j)}} - U_{\theta_{(i,\ j-1)}}\right), \tag{5}$$

$$AU_{\theta_{(i-1,\ j)}} + BU_{\theta_{(i,\ j)}} + CU_{\theta_{(i+1,\ j)}} = D, \tag{6}$$

$$A'\Phi_{\theta(i-1,\ j)} + B'\Phi_{\theta(i,\ j)} + C'\Phi_{\theta(i+1,\ j)} = D', \tag{7}$$

with boundary conditions

$$\begin{aligned} &U_{\theta_{(i,\ j)}} = 0,\ U_{r_{(i,\ j)}} = 0,\ \Phi_{(i,\ j)} = 1 \text{ at } R_j = 0, \\ &U_{\theta_{(i,\ j)}} \to 0,\ \Phi_{(i,\ j)} \to 0 \text{ as } R_j \to \infty. \end{aligned} \tag{8}$$

2.2 *Evaporation region*

The evaporation zone is depicted as an extremely thin interface that divides the hydrosphere and the atmosphere, and at which the exchange of mass, momentum, and energy occurs. The model assumes that the flow in this region is laminar, incompressible, and fully developed. The assumption of local thermal equilibrium between the liquid and gas phases is made; thus, only one temperature field is needed for describing the temperature in the interfacial zone and for ensuring a continuous temperature match at the trans-boundaries. The variations in density in the evaporation region are assumed to be dependent on pressure, and they are, therefore, included in the governing equations. As a result, the Boussinesq approximation is not applied since it would not be able to adequately represent the pressure-induced density variations which are very important for the modeling of the buoyancy effects driven by evaporation. Using the method of Reference [40], the non-dimensional version of the evaporation region model corresponding to this approach is introduced below.

$$\frac{\partial \hat{u}_r}{\partial \hat{r}} + \frac{1}{\sin\hat{\theta}}\frac{\partial\left(\sin\hat{\theta}\hat{u}_\theta\right)}{\partial\hat{\theta}} = 0, \tag{9}$$

$$\hat{u}_r\frac{\partial\hat{u}_\theta}{\partial\hat{r}} + \hat{u}_\theta\frac{\partial\hat{u}_\theta}{\partial\hat{\theta}} = \frac{\partial}{\partial\hat{r}}\left(e^{\lambda_E\psi}\frac{\partial\hat{u}_\theta}{\partial\hat{r}}\right) \pm \mathrm{Gr}_E\,\phi\cos\gamma, \tag{10}$$

$$\hat{u}_r\frac{\partial\phi}{\partial\hat{r}} + \hat{u}_\theta\frac{\partial\phi}{\partial\theta} = \frac{1}{\mathrm{Pr}_E}\frac{\partial}{\partial\hat{r}}\left(e^{\lambda_E\psi}\frac{\partial\phi}{\partial\hat{r}}\right), \tag{11}$$

subject to boundary conditions

$$\hat{u}_\theta = 0,\ \hat{u}_r = 0,\ \phi = 1,\ \text{ at } \hat{r} = 0,$$

$$\hat{u}_\theta \to 0, \quad \phi \to 0, \quad \text{as } \hat{r} \to \infty, \tag{12}$$

$$\hat{r} = \frac{r-b}{b},\ \hat{u}_r = \frac{bu_r}{\nu},\ \hat{u}_\theta = \frac{bu_\theta}{\nu},\ \hat{\theta} = \theta,\ \phi = \frac{T-T_A}{T_E-T_A},\ \psi = \frac{P-P_A}{P_E-P_A}, \tag{13}$$

where $Gr_E = \dfrac{g\beta\,(T_E - T_A)\,b^3}{\upsilon^2}$ and $\rho(P) = \rho_\infty e^{\left[\frac{(P-P_A)}{K}\right]}$ with $\dfrac{1}{K}$ is bulk modulus by [11].

2.2.1 *Methodological framework and computational strategy*

To investigate the current problem, we employed the finite difference methodology, which is widely utilized in related domains. The governing equations (9)–(12) are transformed into a more acceptable form using primitive variable formulation. The finite difference methodology is used to discretize differential equations, which are then converted into algebraic equations. To carry out the aforementioned technique, we followed [39], which generated the algebraic equations with boundary conditions presented below.

$$U_{r_{(i+1,\ j)}} = U_{r_{(i-1,\ j)}} + \frac{R_j}{4}\left(U_{\theta_{(i+1,\ j)}} - U_{\theta_{(i-1,\ j)}}\right) - \Delta R U_{\theta_{(i,\ j)}} - 2\Delta R\Theta_i U_{\theta_{(i,\ j)}}\cot\Theta_i - \frac{2\Delta R\Theta_i}{\Delta\Theta}\left(U_{\theta_{(i,\ j)}} - U_{\theta_{(i,\ j-1)}}\right), \tag{14}$$

$$AU_{\theta_{(i-1,\ j)}} + BU_{\theta_{(i,\ j)}} + CU_{\theta_{(i+1,\ j)}} = D, \tag{15}$$

$$A'\Phi_{\theta_{(i-1,\ j)}} + B'\Phi_{\theta_{(i,\ j)}} + C'\Phi_{\theta_{(i+1,\ j)}} = D', \tag{16}$$

$$U_{\theta_{(i,\ j)}} = 0,\ U_{r_{(i,\ j)}} = 0,\ \Phi_{(i,j)} = 1 \text{ at } R_j = 0,$$

$$U_{\theta_{(i,\ j)}} \to 0,\ \Phi_{(i,\ j)} \to 0 \text{ as } R_j \to \infty. \tag{17}$$

2.3 *Atmosphere region*

The atmospheric zone is assumed to be concentrated with nanoparticles. The Buongiorno Model is utilized to study the properties of nanoparticles in this region. Corresponding dimensional equations using [40] are:

$$\frac{\partial u_r}{\partial r} + \frac{1}{d\sin\theta}\frac{\partial \sin\theta u_\theta}{\partial\theta} = 0, \tag{18}$$

$$\rho(T)\left(u_r\frac{\partial u_\theta}{\partial r} + \frac{u_\theta}{d}\frac{\partial u_\theta}{\partial\theta}\right) = \frac{\partial}{\partial r}\left(\mu(T)\frac{\partial u_\theta}{\partial r}\right) \pm g\beta\rho_\infty(T-T_\infty)\cos\gamma \pm g\beta_C\rho_\infty(C-C_\infty)\cos\gamma, \tag{19}$$

$$u_r\frac{\partial T}{\partial r}+\frac{u_\theta}{d}\frac{\partial T}{\partial \theta}=\frac{1}{C_p\rho(T)}\frac{\partial}{\partial r}\left(k(T)\frac{\partial T}{\partial r}\right)+\tau\left[\mathrm{D}_B\frac{\partial C}{\partial r}\frac{\partial T}{\partial r}+\frac{\mathrm{D}_T}{T_\infty}\left(\frac{\partial T}{\partial r}\right)^2\right], \tag{20}$$

$$u_r\frac{\partial C}{\partial r}+\frac{u_\theta}{d}\frac{\partial C}{\partial \theta}=D_B\frac{\partial^2 C}{\partial r^2}+\frac{D_T}{T_\infty}\frac{\partial^2 T}{\partial r^2}, \tag{21}$$

in accordance with boundary conditions

$$\begin{gathered} u_\theta=0,\ u_r=0,\ T=T_A,\ C=C_A \text{ at } r=d,\ \theta\geq 0,\\ u_\theta\to 0,\ T\to T_\infty,\ C\to C_\infty \text{ as } r\to\infty,\ \theta\geq 0. \end{gathered} \tag{22}$$

The dimensionless form of Eqs (18)–(22) is given below:

$$\frac{\partial \hat{u}_r}{\partial \hat{r}}+\frac{1}{\sin\hat{\theta}}\frac{\partial\left(\sin\hat{\theta}\hat{u}_\theta\right)}{\partial\hat{\theta}}=0, \tag{23}$$

$$(1-\beta_A\phi)\left(\hat{u}_r\frac{\partial\hat{u}_\theta}{\partial\hat{r}}+\hat{u}_\theta\frac{\partial\hat{u}_\theta}{\partial\hat{\theta}}\right)=\frac{\partial}{\partial\hat{r}}\left[(1+\varepsilon_A\phi)\frac{\partial\hat{u}_\theta}{\partial\hat{r}}\right]\pm\mathrm{Gr}_T\,\phi\cos\gamma\pm\mathrm{Gr}_C\,\xi\cos\gamma, \tag{24}$$

$$(1-\beta_A\phi)\left(\hat{u}_r\frac{\partial\phi}{\partial\hat{r}}+\hat{u}_\theta\frac{\partial\phi}{\partial\theta}\right)=\frac{1}{\mathrm{Pr}_A}\frac{\partial}{\partial\hat{r}}\left((1+\eta_A\phi)\frac{\partial\phi}{\partial\hat{r}}\right)+N_b(1-\beta_A\phi)\frac{\partial\xi}{\partial\hat{r}}\frac{\partial\phi}{\partial\hat{r}}\quad+N_t(1-\beta_A\phi)\left(\frac{\partial\phi}{\partial\hat{r}}\right)^2, \tag{25}$$

$$\hat{u}_r\frac{\partial\xi}{\partial\hat{r}}+\hat{u}_\theta\frac{\partial\xi}{\partial\theta}=\frac{1}{\mathrm{Sc}}\left(\frac{\partial^2\xi}{\partial\hat{r}^2}+\frac{N_t}{N_b}\frac{\partial^2\phi}{\partial\hat{r}^2}\right), \tag{26}$$

where, $N_b=\dfrac{(\rho C_p)_P D_B(C_A-C_\infty)}{\nu(\rho C_p)_f}$, $N_t=\dfrac{(\rho C_p)_P D_T(T_A-T_\infty)}{\nu T_\infty(\rho C_p)_f}$, $Gr_T=\dfrac{g\beta(T_A-T_\infty)d^3}{\upsilon^2}$, $Gr_C=\dfrac{g\beta_C(C_A-C_\infty)d^3}{\upsilon^2}$ and $Sc=\dfrac{\nu}{D_B}$ are Brownian motion parameter, thermophoresis parameter, thermal Grashof number, concentration Grashof number and Schmidth number respectively.

Subject to boundary conditions

$$\begin{gathered} \hat{u}_\theta=0,\quad \hat{u}_r=0,\quad \phi=1,\quad \xi=1 \text{ at } \hat{r}=0,\\ \hat{u}_\theta\to 0,\quad \phi\to 0,\quad \xi\to 0 \text{ at } \hat{r}\to\infty, \end{gathered} \tag{27}$$

with variables

$$\hat{r} = \frac{r-d}{d}, \quad \hat{u}_r = \frac{du_r}{v_f}, \quad \hat{u}_\theta = \frac{du_\theta}{v_f}, \quad \hat{\theta} = \theta, \quad \phi = \frac{T-T_\infty}{T_A-T_\infty}, \quad \xi = \frac{C-C_\infty}{C_A-C_\infty}. \tag{28}$$

2.3.1 *Methodological framework and computational strategy*

To explore the current problem, we used the finite difference methodology. The governing equations (18)–(21) are changed into a more suitable form by employing primitive variable formulation. The finite difference methodology is utilized to discretize differential equations before converting them into algebraic equations. To carry out the aforementioned procedure, we used [39], which created the algebraic equations and boundary conditions shown below.

$$U_{r_{(i+1,\ j)}} = U_{r_{(i-1,\ j)}} + \frac{R_j}{4}\left(U_{\theta_{(i+1,\ j)}} - U_{\theta_{(i-1,\ j)}}\right) - \Delta R U_{\theta_{(i,\ j)}} - 2\Delta R\Theta_i U_{\theta_{(i,\ j)}} \cot\Theta_i - \frac{2\Delta R\Theta_i}{\Delta\Theta}\left(U_{\theta_{(i,\ j)}} - U_{\theta_{(i,\ j-1)}}\right), \tag{29}$$

$$AU_{\theta_{(i-1,\ j)}} + BU_{\theta_{(i,\ j)}} + CU_{\theta_{(i+1,\ j)}} = D, \tag{30}$$

$$A'\Phi_{\theta_{(i-1,\ j)}} + B'\Phi_{\theta_{(i,\ j)}} + C'\Phi_{\theta_{(i+1,\ j)}} = D', \tag{31}$$

$$A''\xi_{(i-1,\ j)} + B''\xi_{(i,\ j)} + C''\xi_{(i+1,\ j)} = D'', \tag{32}$$

with discretized boundary conditions

$$\begin{aligned} &U_{\theta_{(i,\ j)}} = 0, \quad U_{r_{(i,\ j)}} = 0, \quad \Phi_{(i,\ j)} = 1, \quad \xi_{(i,\ j)} = 1, \text{ at } R_j = 0, \\ &U_{\theta_{(i,\ j)}} \to 0, \quad \Phi_{(i,\ j)} \to 0, \quad \xi_{(i,\ j)} \to 0, \text{ as } R_j \to \infty. \end{aligned} \tag{33}$$

2.3.2 *Numerical accuracy and advantages*

The present study employs the Finite Difference Method to solve the coupled heat and mass transfer equations in the hydrosphere-evaporation-atmosphere system. This method is particularly suitable due to its simplicity, ability to handle structured grids, and flexibility in applying complex boundary conditions. By discretizing the governing equations into algebraic forms, this method accurately captures variations in velocity, temperature, and nanoparticle concentration across the three regions. The resulting tridiagonal systems are solved iteratively using the Gaussian elimination method, which efficiently reduces computational cost and memory usage. The numerical algorithm was implemented in FORTRAN 95, a language well suited for array-based scientific computations.

The computational domain is discretized on a uniform 81×81 grid, with $\Delta R = 0.05$ and $\Delta\Theta = 0.05$. Iterations are performed until the convergence criterion:

$$\max\left|U_{\theta_{(i,\ j)}}\right| + \max\left|U_{r_{(i,\ j)}}\right| + \max\left|\Phi_{(i,\ j)}\right| < \varepsilon, \text{ where } \varepsilon \in= 10^{-5},$$

is satisfied. Variations in the computed non-dimensional temperature and velocity fields remain below 10^{-5}, ensuring numerical stability and precision up to five significant digits. The prescribed boundary conditions are fully satisfied throughout the computational domain, as confirmed both graphically (Figures 2–7) and in tabular form. Post-processing

and visualization were performed using Tecplot 360 to examine velocity distributions, thermal fields, and heat transfer patterns in detail.

The Finite Difference Method offers several advantages for this study: it provides accurate resolution of steep gradients in velocity, temperature, and concentration; it allows precise control over convergence and numerical stability; and it is computationally efficient when combined with iterative solvers for sparse matrices. Overall, the combination of this method, validated boundary conditions, controlled convergence, and a uniform grid ensures that the results are numerically robust, physically consistent, and reliable for analyzing heat and mass transfer at the hydrosphere-atmosphere interface.

3. Results and discussion

In this study, the effects of atmospheric nanoparticles concentration using Buongiorno's Model, pressure dependent density at interface, and hydrosphere with viscous dissipation effects all considered in relation to the thermal exchanges among the hydrosphere and atmosphere, which serve as the foundation for controlling Earth's climate system. An effective coding scheme is developed with the help of the primitive variable formulation, and the resulting equations are discretized via Gaussian elimination method using Laher Fortran-95. The resulting data is imported into Tecplot 360, where it is shown as tables, graphs, and contour plots. The results obtained for each of the regions under investigation are separated into three distinct regions the Hydrosphere Zone, the Evaporation Zone, and the Atmosphere Zone for the sake of clarity.

3.1 *Hydrosphere zone*

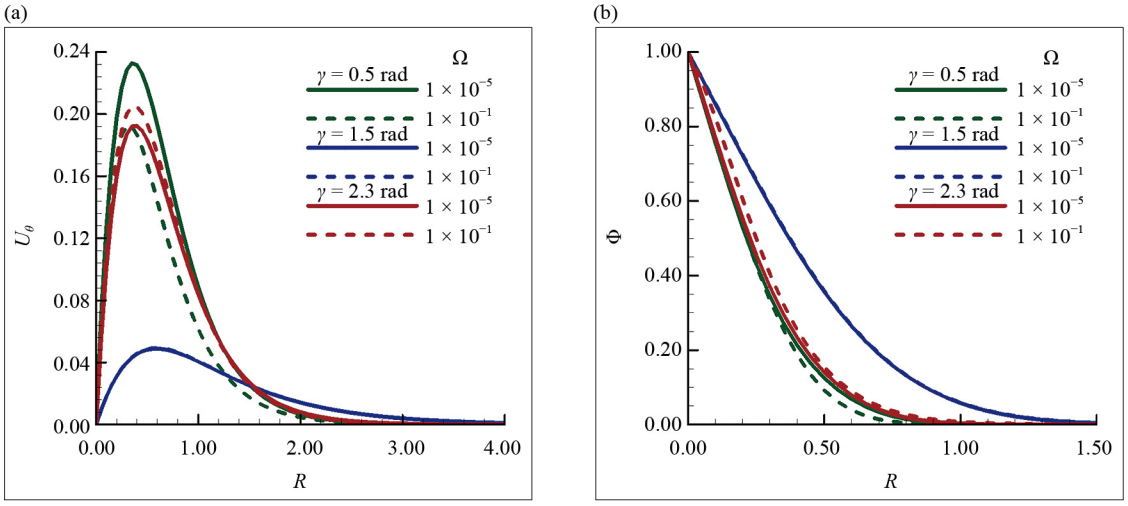

Figure 2. Heat transfer profile and velocity profile for different viscous dissipation parameter values $\Omega = 1 \times 10^{-5}$ and 1×10^{-1} when $Pr_H = 7.0$, $\gamma = 0.5$, 1.5 and 2.3, $Gr_H = 8.0$

Figure 2a illustrate the influence of viscous dissipation Ω on velocity distribution under different angular positions γ. At lower $\gamma = 0.5$ radian, the velocity peaks are highest, indicating strengthen convective momentum transfer near the hydrosphere surface. As γ increases to $\gamma = 2.3$ radians, the peak velocity drops and the flow spreads more slowly, representing weaker convection and a thicker, more stable boundary layer. A higher value of Ω corresponds to stronger internal friction within the fluid, which resists motion and causes energy loss. As a result, the peak velocity drops and the profile flattens. This suppression effect is more significant at $\gamma = 0.5$ radian, where convection would otherwise be strongest. From a climate perspective, enhanced viscous dissipation near the hydrosphere surface may reduce the vertical and radial transport of heat, limiting the efficiency of natural convection. This can contribute to localized thermal buildup and influence broader atmospheric circulation patterns that regulate climate variability. The thermal distribution showed in

Figure 2b discloses the influence of angular position and viscous dissipation parameter on the behavior of the temperature in hydrosphere zone boundary layer. For all scenarios, the dimensionless temperature Φ decreases with radial distance R, but the rate of this decay varies significantly with angular position. At $\gamma = 0.5$ radian, the temperature drops quickly, signifying a steep thermal gradient and efficient heat transfer away from the surface. As the angular position increases to $\gamma = 1.5$ radians, the profile becomes flatter, suggesting slower thermal diffusion and greater heat retention. This implies a thicker thermal boundary layer at higher angles, which is often associated with weaker convective transport. An increase in Ω results in raised temperature profiles for all angular positions. This activity can be attributed to the internal generation of heat through viscous friction, which contributes additional energy to the system. Subsequently, higher viscous dissipation reduces the rate of heat loss, especially near the surface region, altering the thermal boundary layer thickness. In Figures 2 and 3 The range of $R \approx 1.2 - 1.4$ at which the overlap is seen is a result of the local balancing of the viscous dissipation and buoyancy forces, thus leading to the least sensitivity of the parameter to changes. The corresponding period suggests a mixing region between the flow of the boundary layer and the still outer parts.

3.2 *Evaporation zone*

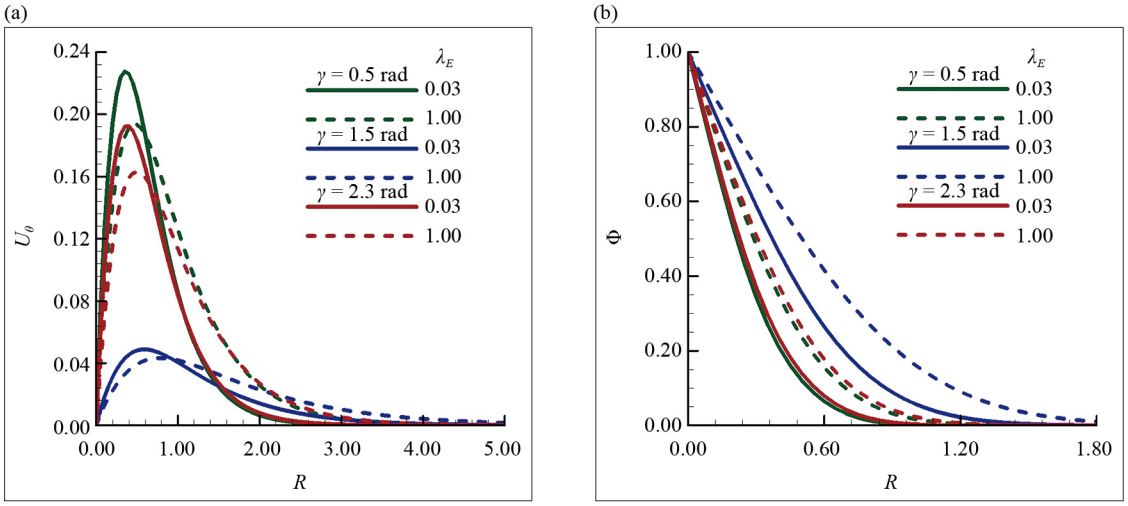

Figure 3. Heat transfer profile and velocity profile for different density variation parameter values $\lambda_E = 0.03$ and 1.00, when $Pr_E = 7.0$, $\gamma = 0.5,\ 1.5,\ 2.3$ rad, $Gr_E = 8.0$

Figure 3a illustrates the dimensionless velocity U_θ as a function of radial distance R for several angular positions and values of the density variation parameter. The results exhibit that both angular location and density stratification significantly affect the flow behavior. At lower angular positions $\gamma = 0.5$ radian, the velocity profiles exhibit higher peaks and sharper slopes, demonstrating stronger natural convection and thinner boundary layers. At the position $\gamma = 1.5$ radian, the peak velocity weakens and the profile broadens, implying a gradual weakening of convective transport and a more stabilized flow regime. The influence of the density variation parameter λ_E is also noticeable. For $\lambda_E = 0.03$, which represents weak density variation (nearly constant density), the buoyancy forces are more efficient, resulting in higher flow velocities and enhanced convective strength. In contrast, when $\lambda_E = 1.00$, demonstrating stronger density variation, the convective motion is suppressed. This occurs because greater density gradients increase stratification and reduce the efficiency of buoyancy-driven flow, thereby thickening the boundary layer and lowering the overall momentum transport. In Figure 3b the temperature distribution is shown, the profiles steadily display a monotonic decay from the surface $R = 0$, with the rate and amount of this decrease being sensitive to both angular position and density variation effects. At $\gamma = 0.5$ radian, the temperature drop rapidly, indicating large thermal gradient which implies efficient convective heat transfer. At position $\gamma = 1.5$ radians, the decay become more slow, resulting in uniform distribution and retained temperature over large radial distance. This reflects the development of a thicker thermal boundary layer, where convective

is comparatively weaker. The influence of λ_E is especially noteworthy. For smaller value, the fluid behaves more like negligible density medium increasing buoyancy-driven convection. On the other hand, larger value tends to stabilize the fluid and decrease convection. In the context of climate interaction, such stratified thermal structures may affect the exchange of energy between hydrosphere and atmosphere, decrease mixing, and contribute in warming the certain hydrosphere regions, affecting regional climate stability.

3.3 *Atmospheric zone*

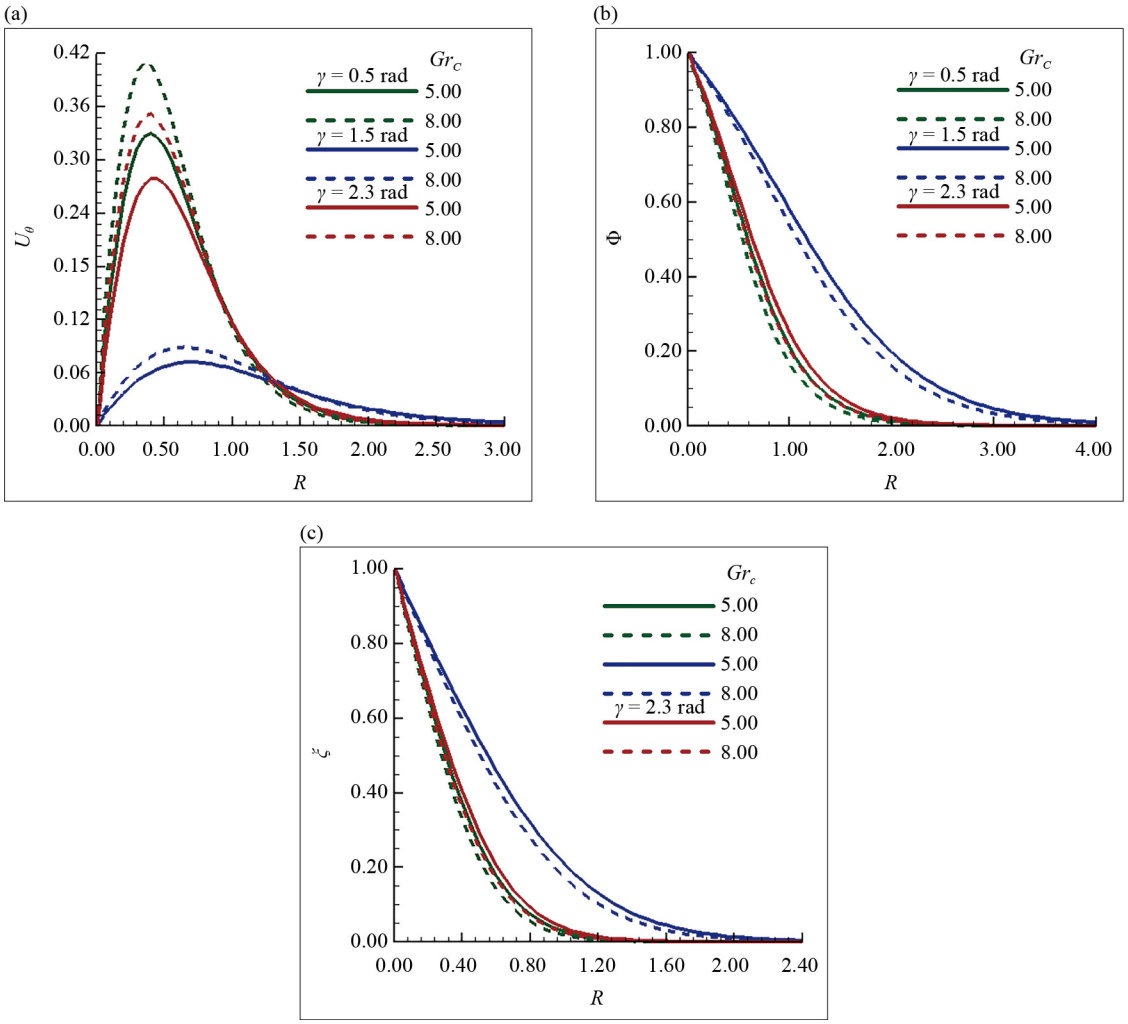

Figure 4. Profiles of concentration, heat transfer, and velocity at different concentration values Grashof's number $Gr_C = 5.00$ and 8.00, when $Pr_A = 0.71$, $\gamma = 0.5$, 1.5 and 2.3 radians, $Gr_T = 1.1$, $\beta_A = 0.03$, $\varepsilon_A = 0.04$, $\eta_A = 0.7$, $N_t = 0.5$, $N_b = 1.5$, $Sc = 1.5$

Figure 4a–c illustrates the variation of the dimensionless velocity, Temperature and concentration profile by means of radial distance, providing the impacts of angular location γ and the concentration Grashof number Gr_C, which describes the buoyancy force encouraged by concentration gradients. (nanoparticles). The outcomes in Figure 4a demonstrate that at the angle $\gamma = 0.5$ radians, the velocity profiles range their highest peak values, reflecting strong natural convection near to the surface, where concentration gradients are more effective in driving buoyant motion. For the position $\gamma = 1.5$ radians, the velocity decreases expressively, indicating weak convection due to geometrical spreading and reduced local gradients. It is also noted that increasing Gr_C leads to rise in peak velocity areas across all positions because enhanced concentration buoyancy promotes convective flow by amplifying the upward force. In the context of climate systems, this behavior is

important for understanding how concentration gradients can deepen natural convection near the hydrosphere atmosphere interface. Regions with stronger buoyancy may exhibit enhanced mixing and vertical transport of heat and mass, which play a vital role in regulating energy exchange and climate feedback mechanisms. In Figure 4b–c, the profiles of temperature and concentration exhibit a decaying trend from origin. At location $\gamma = 0.5$ radians, both profiles drop rapidly, highlighting strengthen convection and for location $\gamma = 1.5$ radians, the profiles are flatter as compared to other locations which shows gradual flow, thicker boundary layer and weak convection. The presence of nanoparticles alters the thermal and mass transport features of the flow. Nanoparticles improve thermal conductivity, which can steepen the temperature gradient near the surface, but their extra mass and interaction with the base fluid can also increase viscous resistance. Overall, the coupled behavior of temperature and nanoparticle concentration profiles shows that angular positioning and concentration impacts play a critical role in governing heat and mass transfer. This has important implications for climate-related studies, where nanoparticle flows and evaporation-driven concentration slopes affect energy exchange in hydrosphere- atmosphere interaction.

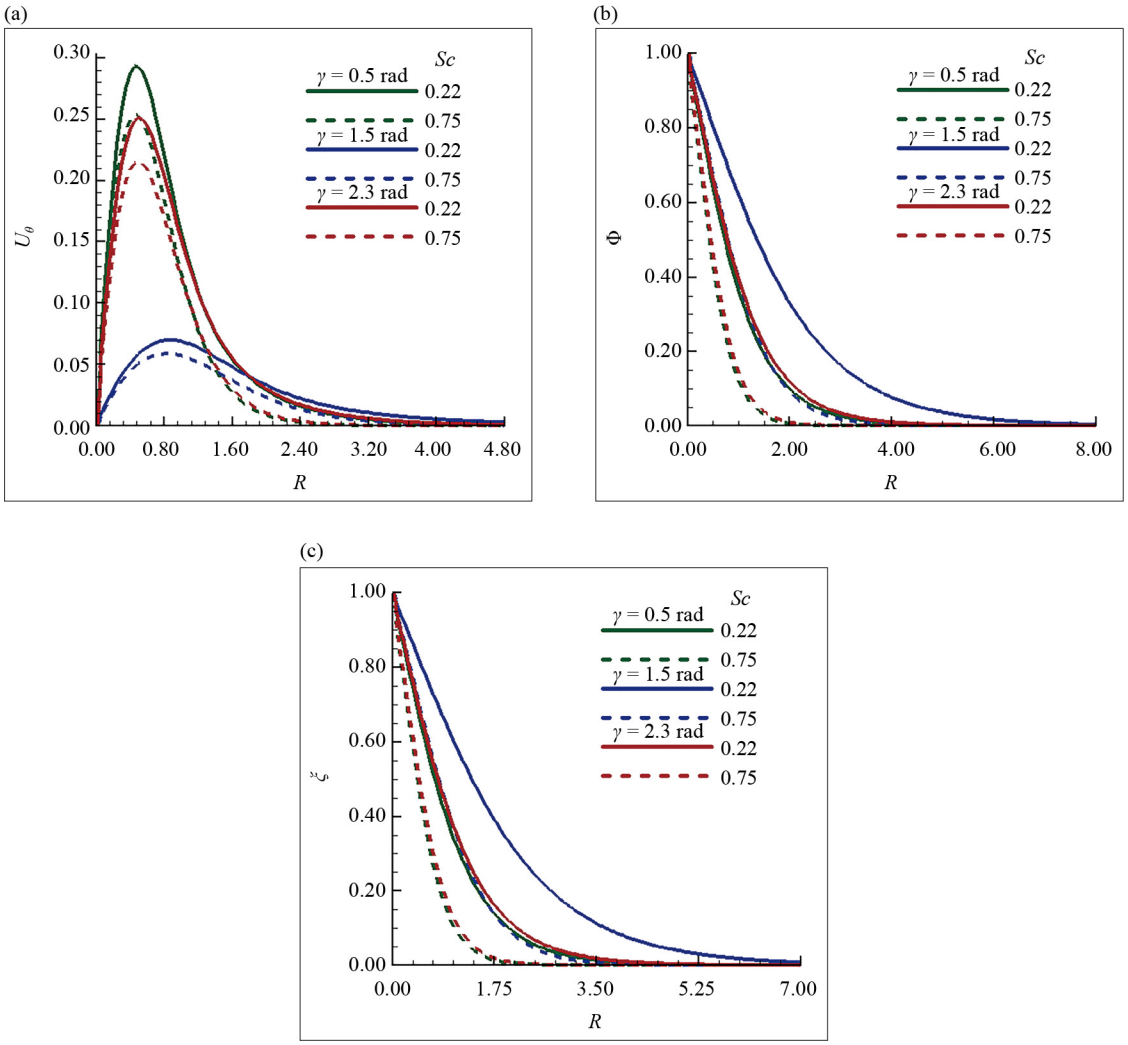

Figure 5. Profiles of concentration, heat transfer, and velocity for various Schmidt number values $Sc = 0.22$ and 0.75, when $Pr_A = 0.71$, $\gamma = 0.5$, 1.5 and 2.3 radians, $Gr_C = 2.0$, $\beta_A = 0.03$, $\varepsilon_A = 0.04$, $\eta_A = 0.7$, $N_t = 0.4$, $N_b = 1.1$, $Gr_T = 1.2$

Figure 5a–c presents the effect of the Schmidt number $Sc = 0.22$ and 0.75 and angular position $\gamma = 0.5$, 1.5 and 2.3 on the dimensionless velocity, temperature, and nanoparticle concentration profiles. As Schmidt number is the ratio

of momentum diffusivity to mass diffusivity, plays a significant role in determining how nanoparticles affect flow and transport properties. At lower $Sc = 0.22$, nanoparticles diffuse more rapidly, resulting in stronger concentration buoyancy forces that increase the flow velocity and steepen the concentration gradient. This shows the higher peak in the velocity profile and thinner momentum boundary layers, particularly at position $\gamma = 0.5$ radian having strong natural convection. When Sc increases to 0.75, the mass diffusivity decreases implies that nanoparticle movement become slow. This leads to noticeable decline in velocity and expansion of velocity profile, especially seen at $\gamma = 1.5$ radian. The temperature and concentration profiles also reflects the same trend that at low Sc, the thermal gradient is sharper, whereas for high Sc it becomes gradual indicating weaker concentration gradients. Additionally as angular position increases from 0.5 to 1.5 radian, all profiles tend to flatten. This is because the radial driving forces become less effective at higher angular locations due to geometric dispersion and reduced local gradients.

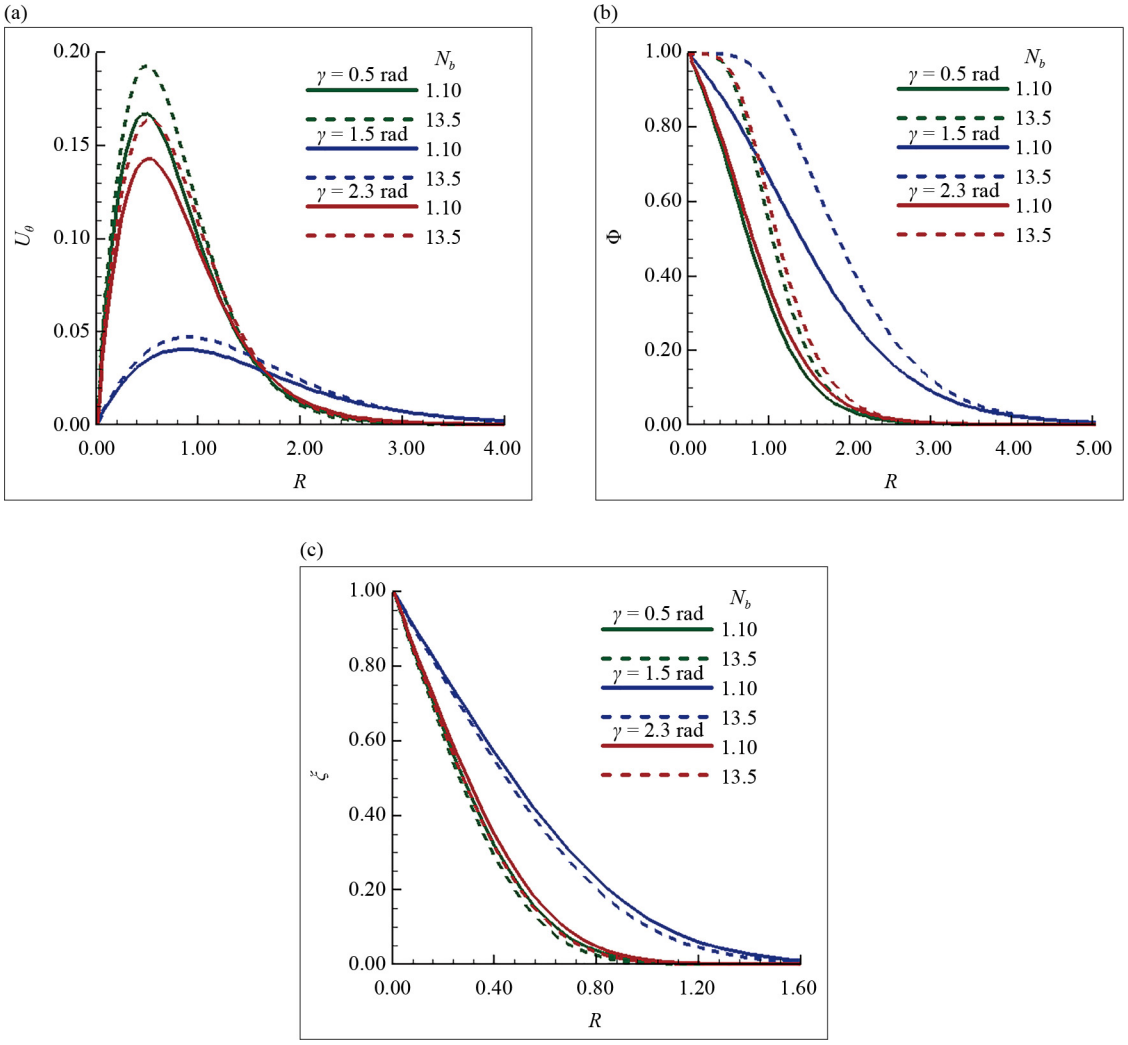

Figure 6. Profiles of concentration, heat transfer, and velocity for various Brownian motion parameter values $N_b = 1.10$ and 13.5, when $Pr_A = 0.71$, $\gamma = 0.5,\ 1.5,\ 2.3$ rad, $Gr_C = 1.5$, $\beta_A = 0.003$, $\varepsilon_A = 0.004$, $\eta_A = 0.5$, $N_t = 0.7$, $Sc = 4.0$, $Gr_T = 1.1$

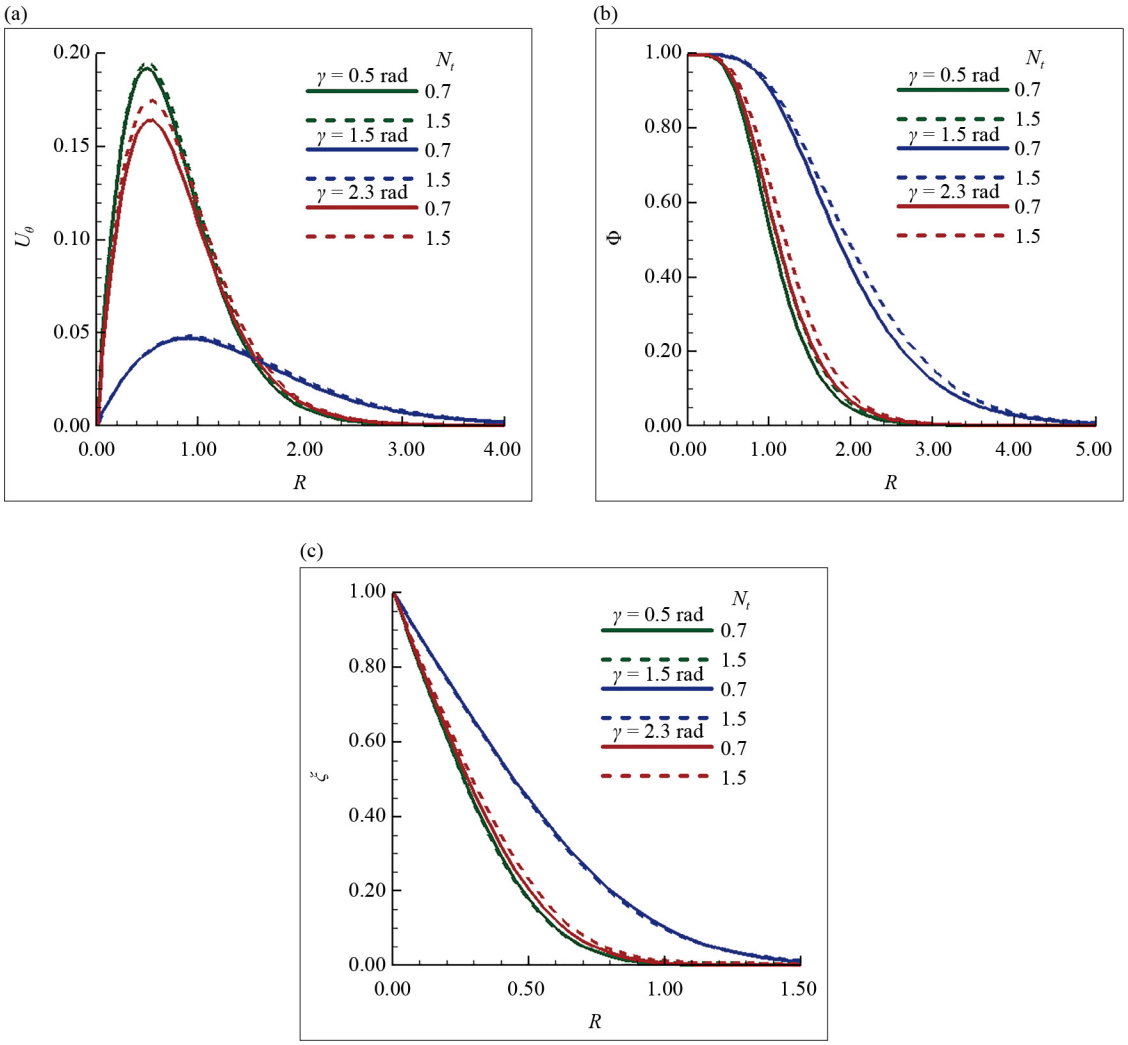

Figure 7. Profiles of concentration, heat transfer, and velocity for various thermophoresis parameter values $N_t = 0.70$ and 1.5, when $Pr_A = 0.71$, $\gamma = 0.5,\ 1.5,\ 2.3$ rad, $Gr_C = 1.5$, $\beta_A = 0.003$, $\varepsilon_A = 0.004$, $\eta_A = 0.5$, $N_b = 12.5$, $Sc = 4.0$, $Gr_T = 1.1$

Figure 6a–c presents the Brownian motion parameter's effect on velocity, temperature and concentration distributionon for angular positions. As N_b increases from 1.10 to 13.5, the temperature profiles exhibit a noteworthy rise, particularly adjacent the surface, highlighting increased heat transfer due to deepened random motion of nanoparticles. The thicker thermal boundary layers and slower temperature decline, particularly at lower angular position $\gamma = 0.5$ radian where convection is stronger. The velocity indicates a slight increase in peak values with higher N_b, as Brownian-induced thermal energy strengthens buoyancy forces. However, this effect lessens at higher $\gamma = 1.5$ radian, where the velocity decreases and the boundary layer widens due to reduced convective movement. In the concentration profiles, increasing γ from 0.5 to 1.5 causes the nanoparticle distribution to flatten, reducing the gradient near the surface. This reflects increased particle diffusion from high-to low-concentration zones. In Figure 7a–c, the effect of the thermophoresis parameter N_t represents the effect of temperature gradients on nanoparticle movement, affecting particles to move from hotter to cooler regions. For increasing N_t, the temperature profiles exhibit a rise, principally near the wall, due to the accumulation of nanoparticles away from the surface, which deepens the near-wall thermal gradient and thickens the thermal boundary layer. For, higher N_t boosts the thermal energy retention and increases concentration gradients by directing nanoparticles away from hot zones. Thicker thermal boundary layers lead to slower temperature fall, especially at angular positions $(\gamma = 1.5$ radian) with higher convection. The velocity shows a minor rise in peak values with larger N_t, although this effect decreases

when $\gamma = 0.5$ radian. Tables 1–3 show the heat and nanoparticle concentration flow rates for various parameters in the atmospheric zone. The heat transfer rate and concentration fluxes with increasing Gr_C, Gr_T and Sc are growing for all positions $\gamma = 0.5,\ 1.5$ and 2.3 radians However, for the parameters $N_b,\ N_t,\ \beta_A,\ \eta_A$ and ε_A the rate of heat transfer and rate of concentration show decreasing behaviour for increasing parameter's values for all angular positions $\gamma = 0.5,\ 1.5$ and 2.3 radians.

Table 1. Concentration rate and heat transfer for various parameter values in the atmospheric region at position $\gamma = 0.5$ radian

Gr_C	Gr_T	Sc	N_b	N_t	β_A	η_A	ε_A	Heat flux $\left(\frac{\partial \Phi}{\partial R}\right)_{R=0}$	Nanoparticles flux $\left(\frac{\partial \xi}{\partial R}\right)_{R=0}$
5.0	-	-	-	-	-	-	-	0.33681	0.79369
8.0	-	-	-	-	-	-	-	0.36984	1.12981
-	1.20	-	-	-	-	-	-	0.27930	0.64237
-	1.70	-	-	-	-	-	-	0.31297	0.92660
-	-	0.22	-	-	-	-	-	0.33948	0.36916
-	-	0.75	-	-	-	-	-	0.34677	0.65914
-	-	-	1.10	-	-	-	-	0.26075	0.76717
-	-	-	13.5	-	-	-	-	0.00150	1.31025
-	-	-	-	0.7	-	-	-	0.00381	0.77495
-	-	-	-	1.5	-	-	-	0.00190	1.32733
-	-	-	-	-	0.007	-	-	0.00388	0.77539
-	-	-	-	-	0.050	-	-	0.00290	1.31599
-	-	-	-	-	-	2.50	-	0.29916	0.76302
-	-	-	-	-	-	7.50	-	0.29022	1.28507
-	-	-	-	-	-	-	0.008	0.26049	0.76623
-	-	-	-	-	-	-	0.700	0.24468	1.13658

Table 2. Concentration rate and heat transfer for various parameter values in the atmospheric region at position $\gamma = 1.5$ radian

Gr_C	Gr_T	Sc	N_b	N_t	β_A	η_A	ε_A	Heat flux	Nanoparticles flux
5.0	-	-	-	-	-	-	-	0.17962	0.42527
8.0	-	-	-	-	-	-	-	0.19724	0.60938
-	1.20	-	-	-	-	-	-	0.14910	0.34529
-	1.70	-	-	-	-	-	-	0.16735	0.49944
-	-	0.22	-	-	-	-	-	0.18412	0.20296
-	-	0.75	-	-	-	-	-	0.18549	0.35447
-	-	-	1.10	-	-	-	-	0.13898	0.41452
-	-	-	13.5	-	-	-	-	0.00088	0.70903
-	-	-	-	0.7	-	-	-	0.00207	0.41491
-	-	-	-	1.5	-	-	-	0.00111	0.71789
-	-	-	-	-	0.007	-	-	0.00210	0.41514
-	-	-	-	-	0.050	-	-	0.00167	0.71217
-	-	-	-	-	-	2.50	-	0.15977	0.41133
-	-	-	-	-	-	7.50	-	0.15484	0.47346
-	-	-	-	-	-	-	0.008	0.13884	0.41403
-	-	-	-	-	-	-	0.700	0.13081	0.61480

Table 3. Concentration rate and heat transfer for various parameter values in the atmospheric region at position $\gamma = 2.3$ radian

Gr_C	Gr_T	Sc	N_b	N_t	β_A	η_A	ε_A	Heat flux	Nanoparticles flux
5.0	-	-	-	-	-	-	-	0.31444	0.74116
8.0	-	-	-	-	-	-	-	0.34526	1.05611
-	1.20	-	-	-	-	-	-	0.26074	0.59985
-	1.70	-	-	-	-	-	-	0.29226	0.86642
-	-	0.22	-	-	-	-	-	0.31739	0.34505
-	-	0.75	-	-	-	-	-	0.32395	0.61564
-	-	-	1.10	-	-	-	-	0.24342	0.71666
-	-	-	13.5	-	-	-	-	0.00143	1.22559
-	-	-	-	0.7	-	-	-	0.00358	0.72365
-	-	-	-	1.5	-	-	-	0.00180	1.24201
-	-	-	-	-	0.007	-	-	0.00364	0.72406
-	-	-	-	-	0.050	-	-	0.00274	1.23160
-	-	-	-	-	-	2.50	-	0.27927	0.71264
-	-	-	-	-	-	7.50	-	0.27100	1.20142
-	-	-	-	-	-	-	0.008	0.24318	0.71578
-	-	-	-	-	-	-	0.700	0.22850	1.06310

The non-dimensional temperature field Φ has been illustrated through the contour plots presented in Figures 8a–c and 9a–c. The three areas—the hydrosphere, evaporation zone, and atmosphere—are represented by concentric regions. The hydrosphere at the core contains the hottest temperature, which then gradually tapers off during the transition to the atmospheric region that is surrounding it. The whole process of temperature gradation is well exemplified with the aid of a color-gradient showing from deep pink-red at the center to blue-green at the border, thus vividly portraying the organized decrease in temperature from the center outwards.

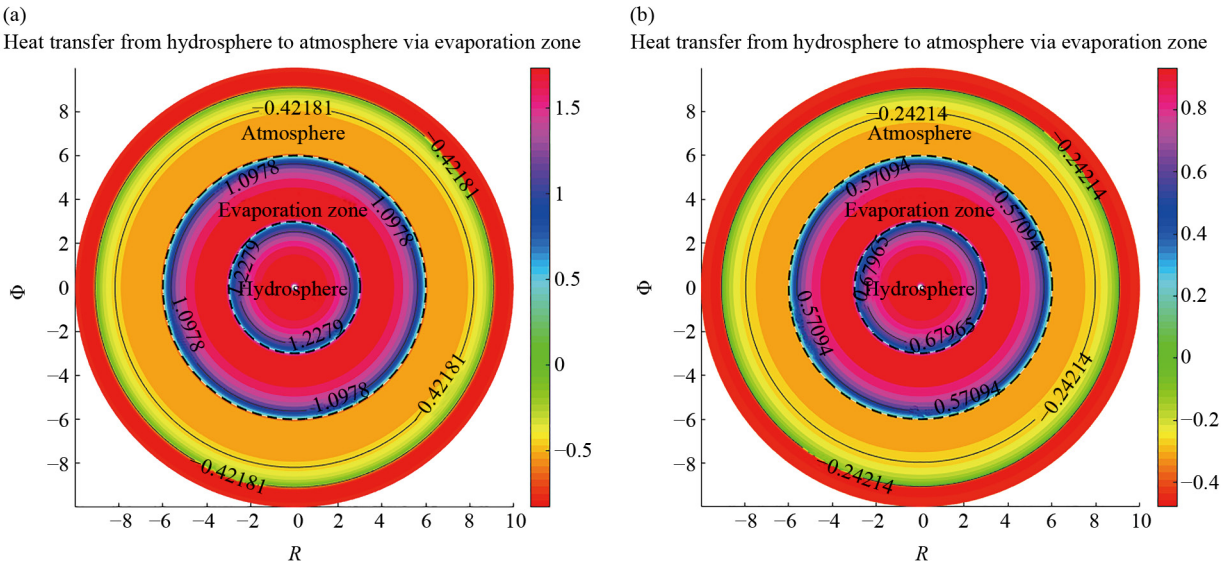

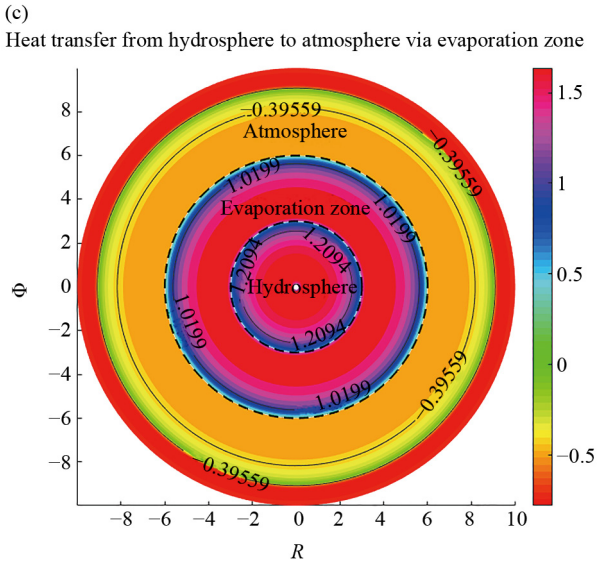

Figure 8. Heat exchange between Hydrosphere and Atmosphere through evaporation region for $Gr = 20$ at various positions (a) $\gamma = 0.5$ radian; (b) $\gamma = 1.5$ radian; (c) $\gamma = 2.3$ radian

In addition to the stated direct and indirect heat transfer, the assigned isotherms are also presented in the plots as one of the strategies to provide the heat transfer direction and relative estimates. Constant temperature lines (isotherms) denote the loci of temperature, which thus offer a quantitative measure valid for examining the temperature gradient between the regions. For instance, the temperature line that delimits the pink area in the hydrosphere in Figure 8a has a Φ value of about 1.2279. This value is very much above the temperatures for the same radial position in the case of the evaporation zone and even more, it is tremendously above the corresponding values of the outer atmosphere region. Thus, it is very clear that the path of a single isotherm from the hydrosphere through the evaporation zone to the atmosphere, by a gradual lowering of Φ, indicates a continuous outward radial heat flow.

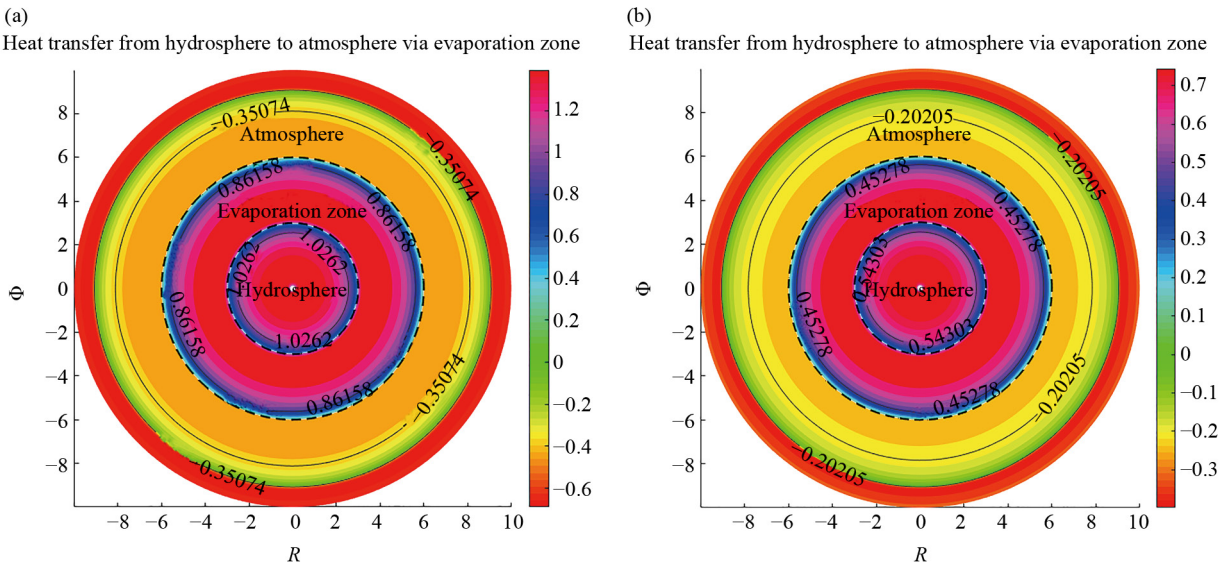

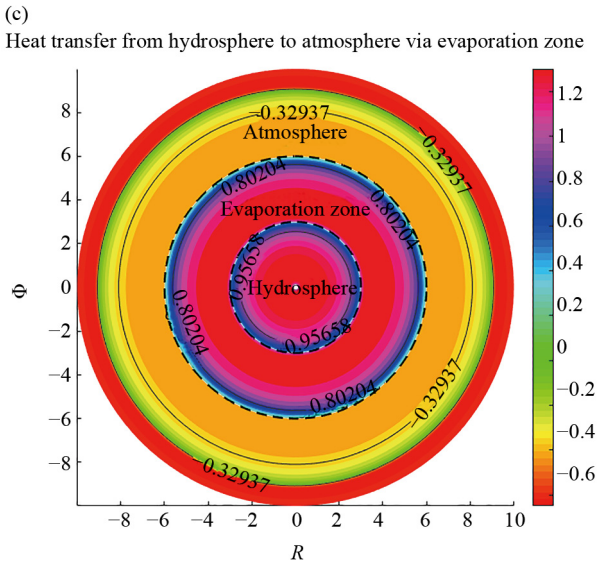

Figure 9. Heat exchange between Hydrosphere and Atmosphere through evaporation region for $Gr = 8$ at various positions (a) $\gamma = 0.5$ radian; (b) $\gamma = 1.5$ radian; (c) $\gamma = 2.3$ radian

In addition, the evaporation zone serves as a transitional layer that regulates the thermal interaction between the highly energetic hydrosphere and the slightly cooler atmosphere. This area acts like a buffer zone that absorbs, redistributes, and slowly dissipates heat, which in turn reduces the temperature differences and maintains the flow of heat transfer. These contour plots not only reveal the intricate spatial distribution of temperature but also allow a clear visual understanding of the basic physics of radial heat transport in this multi-zone system. The main cause of the large gradients is the thermal resistance that exists at the hydrosphere-evaporation and evaporation-atmosphere interfaces, where there are extreme variations in properties. This phenomenon has a physical justification in the heat transfer between the interfaces and the evaporation process.

4. Conclusion

This study investigates the numerical impact on thermal behavior relevant to climate change by examining heat exchange across the hydrosphere (with viscous dissipation), the evaporation zone (with pressure-dependent density), and the atmosphere (with nanoparticle concentration). These regions are coupled through interfacial boundaries. The governing equations were transformed into a dimensionless form using the primitive variable formulation and solved using the finite difference method. The results are presented as profiles and contour plots, showing the influence of various physical parameters, including the thermal Grashof number, concentration Grashof number, viscous dissipation parameter, Brownian motion parameter, and thermophoresis parameter, on velocity, heat, and nanoparticle transport. All parameters significantly affect radial heat transfer and mass transport. A summary of key observations is presented below.

• For lower Schmidt numbers ($Sc = 0.22$) and smaller angular positions ($\gamma = 0.5$ rad), velocity, heat, and nanoparticle transport are enhanced due to stronger buoyancy and higher diffusivity. In contrast, at $\gamma = 1.5$ rad and $Sc = 0.22$, convective transport is suppressed, leading to a thicker boundary layer and reduced thermal exchange across the hydrosphere and atmosphere.

• For the Brownian motion parameter ($N_b = 13.7$) at $\gamma = 0.5$ rad, the velocity profile and nanoparticle concentration reach maximum values, whereas the heat transfer rate attains its maximum at $N_b = 1.10$ for the same angular position. Similarly, for the thermophoresis parameter ($N_t = 1.5$) at $\gamma = 0.5$ rad, the velocity profile and concentration rate are maximized, while the highest heat transfer occurs at $N_t = 0.7$.

• Tables 1–3 make it evident that heat transfer rate for N_t, N_b, Sc and Gr_C is maximum at the angular position $\gamma = 0.5$ radians.

• A negative radial temperature gradient is shown by the contour plots, which show a steady drop in temperature from the hydrosphere to the atmosphere. The physical understanding of heat transport from the warmer hydrosphere into the cooler atmosphere via the evaporation zone is supported by this behavior.

• Overall, it is observed that for all parameter profiles, tables, and contour plots under discussion, the heat transfer rate reaches its maximum at the angular position $\gamma = 0.5$ radians.

The findings of this research provide insight into how the mechanisms of heat exchange between the hydrosphere and the atmosphere can either enhance or suppress thermal transport depending on the physical conditions. It is very important to know these mechanisms in order to determine the areas that are prone to heat accumulation and reduced mixing, which are the main causes of climate warming and variability. Consequently, the current computational framework can assist in refining climate models and in the development of mitigation strategies that are aimed at controlling thermal feedback and energy redistribution.

5. Future recommendations

Numerical exploration that is currently being performed can take multiple routes in the future to make it even more applicable and relevant to different areas of climate-related studies. In particular, future research can focus on:

• The three-dimensional and time-dependent models to obtain a better view of how the hydrosphere and atmosphere interact during transient environmental conditions.

• The integration of more physical mechanisms such as thermal radiation, turbulence effects, and phase-change dynamics may lead to a more thorough and accurate depiction of the heat and mass transfer at the interface.

• Using temperature and concentration dependent thermophysical properties along with different nanoparticle models could also be a way to enhance prediction accuracy.

• In addition, the linking of the suggested numerical framework to observational or climate reanalysis data would make its application even more useful in the context of large-scale climate modeling and mitigation-oriented assessments.

Authors contributions

All authors contributed equally. All authors have read and agreed to the published version of the manuscript.

Data availability statement

The data that support the findings of this study are available from the corresponding author upon reasonable request.

Acknowledgment

The authors extend their appreciation to Prince Sattam bin Abdulaziz University for funding this research work through the project number (PSAU/2025/01/36908).

Conflict of interest

The authors declare no competing financial interest.

References

[1] Mack LR, Hardee HC. Natural convection between concentric spheres at low Rayleigh numbers. *International Journal of Heat and Mass Transfer*. 1968; 11(3): 387–396. Availavle from: https://doi.org/10.1016/0017-9310(68)90083-5.

[2] Scanlan JA, Bishop EH, Powe RE. Natural convection heat transfers between concentric spheres. *International Journal of Heat and Mass Transfer*. 1970; 13(12): 1857–1872. Available from: https://doi.org/10.1016/0017-9310(70)90089-X.

[3] Kuehn TH, Goldstein RJ. An experimental and theoretical study of natural convection in the annulus between horizontal concentric cylinders. *Journal of Fluid Mechanics*. 1976; 74(4): 695–719. Availavle from: https://doi.org/10.1017/S0022112076002012.

[4] Lee HR, Chen TS, Armaly BF. Natural convection along slender vertical cylinders with variable surface temperature. *Journal of Heat Transfer*. 1988; 110(1): 103–108. Availavle from: https://doi.org/10.1115/1.3250439.

[5] Chamkha AJ. Double-diffusive convection in a porous enclosure with cooperating temperature and concentration gradients and heat generation or absorption effects. *Numerical Heat Transfer: Part A: Applications*. 2002; 41(1): 65–87. Available from: https://doi.org/10.1080/104077802317221447.

[6] Asbik M, Sadki H, Hajar M, Zeghmati B, Khmou A. Numerical study of laminar mixed convection in a vertical saturated porous enclosure: The combined effect of double diffusion and evaporation. *Numerical Heat Transfer: Part A: Applications*. 2002; 41(4): 403–420. Available from: https://doi.org/10.1080/104077802317261245.

[7] Alam MM, Alim MAA, Chowdhury MM. Viscous dissipation effects on MHD natural convection flow over a sphere in the presence of heat generation. *Nonlinear Analysis Modelling and Control*. 2007; 12(4): 447–459. Availavle from: https://doi.org/10.15388/NA.2007.12.4.14676.

[8] Saidi M, Abardeh RH. Air pressure dependence of natural-convection heat transfer. In: *Proceedings of the World Congress on Engineering*. Vol. 2. London, United Kingdom: WCE; 2010. p.1–5.

[9] Sheremet MA. Mathematical simulation of unsteady natural convection inside a sphere. *Computational Thermal Sciences: An International Journal*. 2011; 3(4): 277–278. Availavle from: https://doi.org/10.1615/ComputThermalScien.2011002942.

[10] Khan WA, Aziz A, Uddin N. Buongiorno model for nanofluid Blasius flow with surface heat and mass fluxes. *Journal of Thermophysics and Heat Transfer*. 2013; 27(1): 134–141. Availavle from: https://doi.org/10.2514/1.T3916.

[11] Brutsaert W. *Evaporation Into the Atmosphere: Theory, History and Applications*. Dordrecht: Springer; 1982. Available from: https://doi.org/10.1007/978-94-017-1497-6.

[12] Parveen N, Nath S, Alim MA. Viscous dissipation effect on natural convection flow along a vertical wavy surface. *Procedia Engineering*. 2014; 90: 294–300. Availavle from: https://doi.org/10.1016/j.proeng.2014.11.852.

[13] Garoosi F, Jahanshaloo L, Rashidi MM, Badakhsh A, Ali ME. Numerical simulation of natural convection of the nanofluid in heat exchangers using a Buongiorno model. *Applied Mathematics and Computation*. 2015; 254: 183–203. Availavle from: https://doi.org/10.1016/j.amc.2014.12.116.

[14] Lappa M. A mathematical and numerical framework for the analysis of compressible thermal convection in gases at very high temperatures. *Journal of Computational Physics*. 2016; 313: 687–712. Availavle from: https://doi.org/10.1016/j.jcp.2016.02.062.

[15] Kazemi MA, Nobes DS, Elliott JA. Experimental and numerical study of the evaporation of water at low pressures. *Langmuir*. 2017; 33(18): 4578–4591. Availavle from: https://doi.org/10.1021/acs.langmuir.7b00616.

[16] Mustafa M. MHD nanofluid flow over a rotating disk with partial slip effects: Buongiorno model. *International Journal of Heat and Mass Transfer*. 2017; 108: 1910–1916. Availavle from: https://doi.org/10.1016/j.ijheatmasstransfer.2017.01.064.

[17] Ashraf M, Fatima A. Numerical simulation of the effect of transient shear stress and rate of heat transfer around different positions of sphere in the presence of viscous dissipation. *Journal of Heat Transfer*. 2018; 140(6): 061701. Availavle from: https://doi.org/10.1115/1.4038841.

[18] Ahmad S, Ashraf M, Ali K. Numerical simulation of viscous dissipation in a micropolar fluid flow through a porous medium. *Journal of Applied Mechanics and Technical Physics*. 2019; 60: 996–1004. Availavle from: https://doi.org/10.1134/S0021894419060038.

[19] Iasiello M, Vafai K, Andreozzi A, Bianco N. Hypo-and hyperthermia effects on LDL deposition in a curved artery. *Computational Thermal Sciences: An International Journal*. 2019; 11(1-2): 95–103. Availavle from: https://doi.org/10.1615/ComputThermalScien.2018024754.

[20] Abbas A, Ashraf M, Chu YM, Zia S, Khan I, Nisar KS. Computational study of the coupled mechanism of thermophoretic transportation and mixed convection flow around the surface of a sphere. *Molecules*. 2020; 25(11): 2694. Availavle from: https://doi.org/10.3390/molecules25112694.

[21] Khan A, Ashraf M, Rashad AM, Nabwey HA. Impact of heat generation on magneto-nanofluid free convection flow about sphere in the plume region. *Mathematics*. 2020; 8(11): 2010. Availavle from: https://doi.org/10.3390/math8112010.

[22] Mishra A, Kumar M. Numerical analysis of MHD nanofluid flow over a wedge, including effects of viscous dissipation and heat generation/absorption, using Buongiorno model. *Heat Transfer*. 2021; 50(8): 8453–8474. Availavle from: https://doi.org/10.1002/htj.22284.

[23] Reddy PS, Sreedevi P. Buongiorno's model nanofluid natural convection inside a square cavity with thermal radiation. *Chinese Journal of Physics*. 2021; 72: 327–344.

[24] Khatun S, Nasrin R. Numerical modeling of Buongiorno's nanofluid on free convection: Thermophoresis and Brownian effects. *Journal of Naval Architecture and Marine Engineering*. 2021; 18(2): 217–239. Availavle from: https://doi.org/10.3329/jname.v18i2.54694.

[25] Akhter S, Ashraf M. Darcy-Forchheimer flow of nanofluid with gyrotactic microorganisms using Buongiorno model. *Journal of Porous Media*. 2021; 24(8): 1–21. Availavle from: https://doi.org/10.1615/JPorMedia.2021036551.

[26] Ashraf M, Abbas A, Oztop HF, Nisar KS, Khan I. Computations of mixed convection slip flow around the surface of a sphere: Effects of thermophoretic transportation and viscous dissipation. *Heat Transfer*. 2021; 50(7): 7349–7362. Availavle from: https://doi.org/10.1002/htj.22232.

[27] Ashraf M, Ilyas A, Ullah Z, Ali A. Combined effects of viscous dissipation and magnetohydrodynamic on periodic heat transfer along a cone embedded in porous medium. *Proceedings of the Institution of Mechanical Engineers, Part E: Journal of Process Mechanical Engineering*. 2022; 236(6): 2325–2335. Availavle from: https://doi.org/10.1177/09544089221089135.

[28] Nadeem S, Fuzhang W, Alharbi FM, Sajid F, Abbas N, El-Shafay AS, et al. Numerical computations for Buongiorno nano fluid model on the boundary layer flow of viscoelastic fluid towards a nonlinear stretching sheet. *Alexandria Engineering Journal*. 2022; 61(2): 1769–1778. Availavle from: https://doi.org/10.1016/j.aej.2021.11.013.

[29] Owhaib W, Al-Kouz W. Three-dimensional numerical analysis of flow and heat transfer of bi-directional stretched nanofluid film exposed to an exponential heat generation using modified Buongiorno model. *Scientific Reports*. 2022; 12(1): 10060. Availavle from: https://doi.org/10.1038/s41598-022-13351-6.

[30] Begum Z, Saleem M, Islam SU, Saha SC. Numerical study of natural convection flow in rectangular cavity with viscous dissipation and internal heat generation for different aspect ratios. *Energies*. 2023; 16(14): 5267. Availavle from: https://doi.org/10.3390/en16145267.

[31] Ullah Z, Abbas A, El-Zahar ER, Seddek LF, Akgul A, Hassan AM. Significance of thermal density and viscous dissipation on heat and mass transfer of chemically reactive nanofluid flow along stretching sheet under magnetic field. *Results in Engineering*. 2023; 20: 101413.

[32] Ashraf M, Khan A, Abbas A, Hussanan A, Ghachem K, Maatki C, et al. Finite difference method to evaluate the characteristics of optically dense gray nanofluid heat transfer around the surface of a sphere and in the plume region. *Mathematics*. 2023; 11(4): 908. Availavle from: https://doi.org/10.3390/math11040908.

[33] NematpourKeshteli A, Iasiello M, Langella G, Bianco N. Thermal enhancement techniques for a lobed-double pipe PCM thermal storage system. *Applied Thermal Engineering*. 2023; 233: 121139. Availavle from: https://doi.org/10.1016/j.applthermaleng.2023.121139.

[34] NematpourKeshteli A, Iasiello M, Langella G, Bianco N. Increasing melting and solidification performances of a phase change material-based flat plate solar collector equipped with metal foams, nanoparticles, and wavy wall-Y-shaped surface. *Energy Conversion and Management*. 2023; 291: 117268. Availavle from: https://doi.org/10.1016/j.enconman.2023.117268.

[35] Ramirez R, Ghiassi B, Pineda P, Lourenço PB. Hygro-thermo-mechanical analysis of brick masonry walls subjected to environmental actions. *Applied Sciences*. 2023; 13(7): 4514. Availavle from: https://doi.org/10.3390/app13074514.

[36] Khan AA, Ahmed A, Askar S, Ashraf M, Ahmad H, Khan MN. Influence of the induced magnetic field on second-grade nanofluid flow with multiple slip boundary conditions. *Waves in Random and Complex Media*. 2024; 34(6): 5686–5701.

[37] Ullah F, Ashraf MB. Numerical heat transfer analysis of Carreau nanofluid flow over curved stretched surface with nonlinear effects and viscous dissipation. *International Journal of Thermofluids*. 2024; 24: 100914. Availavle from: https://doi.org/10.1016/j.ijft.2024.100914.

[38] Khan SA, Hayat T, Alsaedi A, Ahmad B. Heat and mass transfer enhancement in nonlinear mixed convective flow: Buongiorno model and melting heat phenomenon. *International Communications in Heat and Mass Transfer*. 2024; 153: 107330. Availavle from: https://doi.org/10.1016/j.icheatmasstransfer.2024.107330.

[39] NematpourKeshteli A, Iasiello M, Langella G, Bianco N. Using metal foam and nanoparticle additives with different fin shapes for PCM-based thermal storage in flat plate solar collectors. *Thermal Science and Engineering Progress*. 2024; 52: 102690. Availavle from: https://doi.org/10.1016/j.tsep.2024.102690.

[40] Nadeem H, Ashraf M, Rasool G, Tao S. Thermophoretic convection with catalytic chemical reaction in source region heat sink in plume: Exploring climate change dynamics in double stratified atmosphere. *Physics of Fluids*. 2025; 37(2): 023320. Availavle from: https://doi.org/10.1063/5.0251484.

[41] Rehman A, Ashraf M, Rasool G, Khan MI. Impact of non-linear motion on convective heat transfer induced by oscillating thermal waves in the presence of heat source and sink. *Nano*. 2025; 21(1): 2550038. Availavle from: https://doi.org/10.1142/S1793292025500389.

[42] Nabwey HA, Ashraf M, Rashad AM. A comprehensive review of convective heat transfer in humid air and its physical perspectives in climate change. *AIP Advances*. 2025; 15(5): 055124. Availavle from: https://doi.org/10.1063/5.0270951.

[43] Imtiaz F, Ashraf M, Rasool G, Abbas K, Ali S. Impact of hybrid nanofluid convective heat transfer on climate change adjacent to the surface of the tilted hemisphere placed in the atmosphere. *Journal of Porous Media*. 2025; 28(10): 101–116. Availavle from: https://doi.org/10.1615/JPorMedia.2025056594.

[44] Iqbal R, Ashraf M, Rasool G, Alqahtani AS, Malik MY, Chamkha AJ. Computational study of the combined impacts of variable density of the hydrosphere and thermal jump in atmosphere on climate change. *Alexandria Engineering Journal*. 2025; 121: 504–514. Availavle from: https://doi.org/10.1016/j.aej.2025.02.108.

[45] Iqbal R, Ashraf M, Shah NA. Impact of temperature dependent thermal conductivity and viscosity of hydrosphere and porous atmosphere on climate change: A numerical prediction. *International Communications in Heat and Mass Transfer*. 2025; 162: 108634. Availavle from: https://doi.org/10.1016/j.icheatmasstransfer.2025.108634.

[46] Shahraki A, Tavakoli A, Mohammadi M, Ebrahimi A, Kianifar A. Enhancing the charging performance of a triplex-tube thermal energy storage system using fins and nanoparticles. *Thermal Science and Engineering Progress*. 2025; 62: 103565. Availavle from: https://doi.org/10.1016/j.tsep.2025.103565.